Lattice-depth measurement using continuous grating atom diffraction

Benjamin T. Beswick,* Ifan G. Hughes,† and Simon A. Gardiner‡
Joint Quantum Centre (JQC) Durham–Newcastle, Department of Physics, Durham University, Durham DH1 3LE, United Kingdom

(Received 10 March 2019; published 16 December 2019)

We propose an approach to characterizing the depths of optical lattices, in which either an atomic gas is given a finite initial momentum or, alternatively, a corresponding "walking" configuration is applied to the optical lattice itself. This leads to high-amplitude oscillations in the zeroth diffraction order which are robust to finite-temperature effects. We present a simplified model yielding an analytic formula describing such oscillations for a gas assumed to be at zero temperature. This model is extended to include atoms with initial momenta detuned from our chosen initial value, before analyzing the full finite-temperature response of the system. Finally, we present a steady-state solution to the finite-temperature system, which in principle makes possible the measurement of both the lattice depth and the initial temperature of the atomic gas from a single common data set.

DOI: 10.1103/PhysRevA.100.063629

I. INTRODUCTION

There is much interest in the precise measurement of optical lattice [1] depths in the field of atomic physics, a particular example being for the accurate determination of transition matrix elements [2–6]. Better knowledge of these can be used to improve the blackbody radiation correction for ultraprecise atomic clocks [7,8] and allows quantitative modeling of atom-light interactions [9]. Other areas of interest include atom interferometry [10,11] and many-body quantum physics [12,13], where knowledge of the lattice depth is essential for interpreting experimental results.

Commonly used lattice-depth measurement schemes include Kapitza-Dirac scattering [13–17], parametric heating [18], Rabi oscillations [19], and, more recently, the sudden phase shift method [20]. In this paper, we are principally concerned with weak lattices ($V \lesssim 0.01E_R$ for any atom, where V is the lattice depth and E_R is the atomic recoil energy—this admittedly is in a regime different from that typical for many-body quantum physics investigations, although some of the ideas presented may be applicable in a general sense). In this context, methods based on multipulse atom diffraction have been explored [21,22], effectively as a refinement of the commonly used Rabi oscillation approach [19], with a view to improving the signal-to-noise ratio in the measurement of the resulting diffraction patterns. In previous work we presented improved models for the expected multipulse diffraction patterns for a given lattice depth and, also, noted that when considering a gas with initial momentum $\hbar K/2$ (where K is twice the wave number of the optical lattice laser) the dynamics took a markedly simple form [23].

In this paper we explore a regime of very simple, analytically tractable dynamics that we believe would be useful for determining optical lattice depths. Like [19], it also considers Rabi oscillations between different Bloch bands when applying a lattice which is continuously present throughout the experimental sequence. The crucial difference is that the chosen regime accesses simple resonant behavior, by virtue of considering the initial momentum distribution to be centered at $\hbar K/2$—or, equivalently, for an initial momentum distribution centered at 0, considering a "walking wave" optical lattice with a characteristic walking velocity of $-v_\phi = -\hbar K/2M$, where M is the atomic mass. We show this also to be more robust to finite-temperature effects than the multipulse approach described in [21] for weak lattices in order to determine matrix elements.

Following this introduction, we describe our model system and experimental considerations in Sec. II. In Sec. III, we introduce a simplified analytic approach for determining the time evolution of the atomic population in the zeroth diffraction order and make a comparison to exact numerical calculations. Finally, in Sec. IV, we present an approximate analytic model for the finite-temperature response of the system and discuss how this may be used to determine both the lattice depth and the initial temperature of the atomic gas.

II. MODEL SYSTEM: ATOMIC GAS IN AN OPTICAL GRATING

A. Experimental setup and Hamiltonian

We consider a two-level atom in an assumed noninteracting Bose-Einstein condensate exposed to a far-off resonance optical grating, the Hamiltonian of which is given by Eq. (1),

$$\tilde{H}_{\mathrm{Latt}} = \frac{\hat{p}^2}{2M} - V\cos(K[\hat{x} + v_\phi t]es), \tag{1}$$

where $\hat{p}$ is the momentum operator along the lattice axis, V is the lattice depth, K is twice the laser wave number k_{L}, M is the atomic mass, and v_ϕ is the phase velocity of the grating in the x direction ($v_\phi = 0$ for a static grating). For the simpler case of a static grating, we consider a BEC initially

*b.t.beswick@durham.ac.uk
†i.g.hughes@durham.ac.uk
‡s.a.gardiner@durham.ac.uk

prepared in a momentum state with $p = \hbar K/2$.[1] As shown in Fig. 1(a), the BEC is diffracted by the static optical grating for a time t, before a time-of-flight measurement interrogates the population of the gas in each of the allowed momentum states. In principle, there is an infinite ladder of such states, with each state separated by integer multiples of $\hbar K$ [24,25], though here we show only the zeroth and first diffraction orders. We note that an initial state $p = \hbar K/2$ can be achieved, for instance, by Bragg diffraction or, equivalently, we may prepare the BEC in a state with $p = 0$ and impart an appropriately tuned time-dependent phase $v_\phi t$ to the standing wave as in Fig. 1(b). We show this equivalency in Sec. II B.

B. Gauge transformations and momentum kicks

The Hamiltonian of Eq. (1) can be transformed to a frame comoving with the walking grating by use of the unitary transformation

$$\hat{U} = \hat{U}_x \hat{U}_p \hat{U}_\alpha = \exp(imv_\phi \hat{x}/\hbar)\exp(-iv_\phi \hat{p}t/\hbar)\exp(i\alpha t/\hbar), \tag{2}$$

where we have chosen $\alpha = Mv_\phi^2/2$ for convenience.[2] Using $\hat{U}_p \hat{x} \hat{U}_p^\dagger = \hat{x} - v_\phi t$ and $\hat{U}_x \hat{p} \hat{U}_x^\dagger = \hat{p} - Mv_\phi$, this transformation yields

$$\hat{H}_{\text{Latt}} = \frac{\hat{p}^2}{2M} - V\cos(K\hat{x}). \tag{3}$$

The Hamiltonian of Eq. (3) describes the system in a frame moving at velocity $-v_\phi$, therefore, a gas moving at velocity $v = 0$ in the moving frame appears to move at velocity $-v_\phi$ in the laboratory frame. Conversely, a gas moving at velocity $v = \hbar K/2M$ in the comoving frame moves at velocity $v = (\hbar K/2M) - v_\phi$ in the laboratory frame. Choosing $v_\phi = 0$ yields the case in Fig. 1(a), while with $v_\phi = \hbar K/2M$, we have the situation shown in Fig. 1(b).

The spatial periodicity of Eq. (3) allows us to invoke Bloch theory [26], by rewriting the momentum operator as follows:

$$(\hbar K)^{-1}\hat{p} = \hat{k} + \hat{\beta}, \tag{4a}$$

$$\hat{k}|(\hbar K)^{-1}p = k + \beta\rangle = k|(\hbar K)^{-1}p = k + \beta\rangle, \tag{4b}$$

$$\hat{\beta}|(\hbar K)^{-1}p = k + \beta\rangle = \beta|(\hbar K)^{-1}p = k + \beta\rangle. \tag{4c}$$

We may speak of $k \in \mathbb{Z}$ as the discrete part of the momentum and $\beta \in (-1/2, 1/2]$ as the continuous part or *quasimomentum* [27] in units of $\hbar K$. Here β is a conserved quantity; as such, only momentum states separated by integer multiples of $\hbar K$ are coupled [24,25]. This simplification allows us to construct the time evolution operator acting on a particular quasimomentum subspace for a lattice pulse of duration t from the lattice Hamiltonian, (3), as

$$\hat{U}(\beta, \tau)_{\text{Latt}} = \exp\left(-i\left[\frac{\hat{k}^2 + 2\hat{k}\beta}{2} - V_{\text{eff}}\cos(\hat{\theta})\right]\tau\right), \tag{5}$$

in which β is simply a scalar value such that overall phases which depend solely on β can be neglected.[3] Here

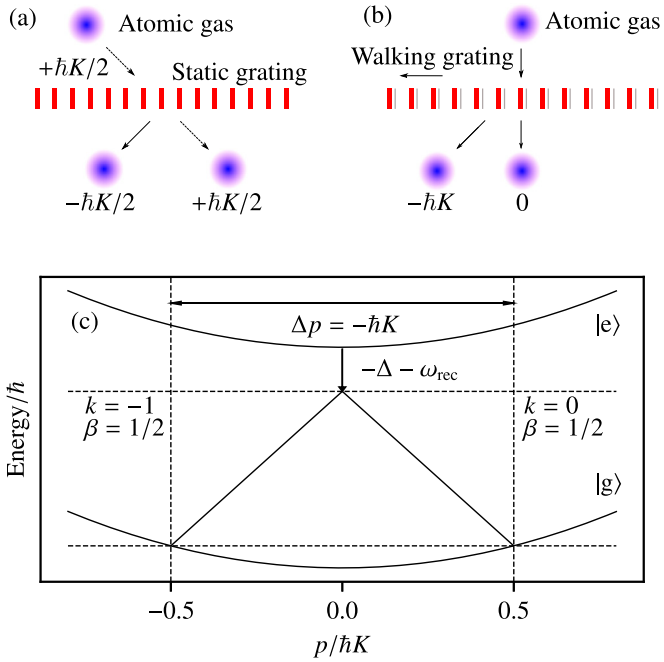

FIG. 1. (a) A BEC initially prepared in the $p = +\hbar K/2$ state, where K is twice the laser wave number k_L, is exposed to a static optical grating, causing it to diffract into an, in principle, infinite number of momentum states separated by integer multiples of $\hbar K$. Here we show only the first diffraction order. Equivalently, the BEC may be prepared in the $p = 0$ state and exposed to a walking grating with a linearly time-dependent phase [see Eq. (1)] as in (b). The dynamics of the setup are identical, though the momenta in the laboratory frame are shifted by $-\hbar K/2$. (c) Semiclassical energy-momentum diagram for a single two-level atom scattering photons from a static optical grating. The atom begins on the ground-state energy parabola, with classical momentum $p = \hbar K/2$, before scattering a photon carrying momentum $p = -\hbar K/2$ and energy $\hbar^2 K^2/2M$ to reach the detuned virtual state above (where Δ is the detuning, i.e., atomic transition frequency minus laser frequency, and $\omega_{\text{rec}} = E_R/\hbar = \hbar K^2/8M$ is the recoil frequency), before undergoing stimulated emission back to the ground state, resulting in a total momentum transfer of $\Delta p = -\hbar K$. This scattering process and its exact reversal are the only processes which semiclassically conserve both the energy and the momentum of the atom-grating system, indicating that population transfer between the $p = \hbar K/2$ and the $p = -\hbar K/2$ states should be the dominant process in the system.

[1]The initial momentum $p = \hbar K/2$ is chosen with a view to creating population oscillations between the zeroth and the first diffraction orders with a strong sinusoidal character. The resulting population dynamics are exactly equivalent to those explored in [23] for this initial condition, due to the fact that the "free" evolution operator, describing the dynamics between successive pulses, collapses to the identity.

[2]This simply ensures that there will be no overall scalar term in the transformed Hamiltonian.

[3]These are only potentially important when considering initial states which include coherent superpositions of different quasimomenta and an observable other than the momentum density, a situation we do not consider in this paper.

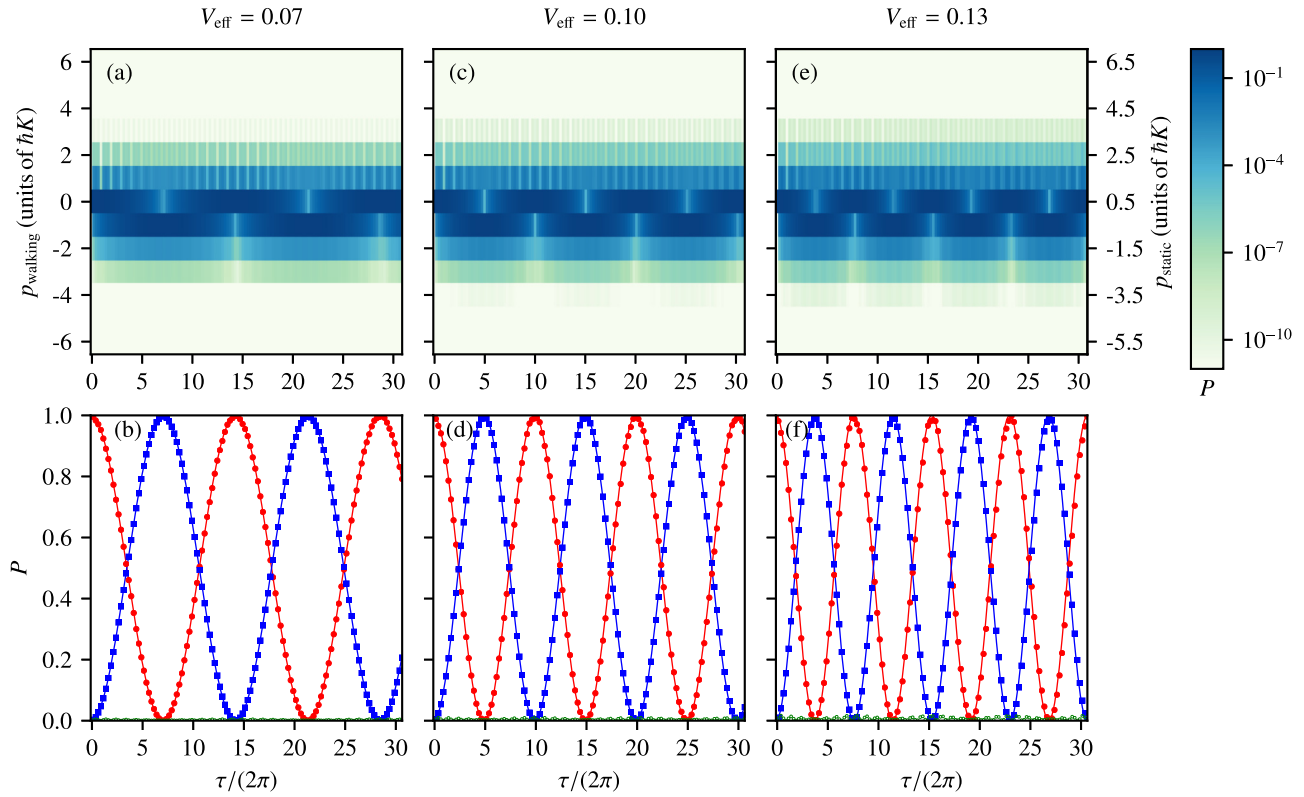

FIG. 2. Time-evolved momentum distributions for an atomic gas initially prepared in the $|k = 0, \beta = 1/2\rangle$ momentum state (corresponding to the $|k = 0, \beta = 0\rangle$ state in the laboratory frame for a walking grating), as calculated numerically on a basis of 2048 momentum states. The top row of false-color plots [(a), (c), (e)] shows the population in the first 13 momentum states, to be read on the logarithmic color bar to the right; a cutoff population of $P_{\rm cutoff} = 10^{-11}$ has been applied to accommodate the log scale. The labels $p_{\rm static}$ and $p_{\rm walking}$ denote the momentum as measured in the laboratory frame for the case of a static and a walking grating, respectively. The bottom row of plots [(b), (d), (f)] shows the time evolution of the population in the $|k = 0\rangle$ (red circles) and $|k = -1\rangle$ (blue squares) states, where the solid line through each curve is given by the analytic solution of Eqs. (8a) and (8b). Also shown is the population in the $|k = 1\rangle$ state (green points). Each column of plots corresponds to a simulation for a fixed value of the effective lattice depth $V_{\rm eff}$; here, from left to right, $V_{\rm eff} = 0.07$, 0.10, and 0.13, respectively.

$V_{\rm eff} = VM/\hbar^2K^2$ is the dimensionless lattice depth, $\hat{\theta} = K\hat{x}$, and $\tau = t\hbar K^2/M = 8\omega_{\rm rec}t$ is the rescaled time.

By using Eq. (5) to calculate $|\psi(\tau)\rangle = \sum_j c_j(\tau)|k = j\rangle$, the population in each discrete momentum state $|k = j\rangle$ following an evolution for a rescaled time of τ is given by the absolute square of the coefficients $P_j(\tau) = |c_j(\tau)|^2$. In this paper we employ the well-known split-step Fourier approach [25,28] to determine $|\psi(\tau)\rangle$, as well as an analytic approach based on a simpler two-state model.

The dynamics of a single atom in the BEC standing-wave system can be understood in terms of the scattering process given by the semiclassical energy diagram in Fig. 1(c) (see also [29–33]). A two-level atom begins in a state with momentum $p = \hbar K/2$, before absorbing a photon with momentum $p = -\hbar K/2$, and subsequently emits a second photon with momentum $p = \hbar K/2$. This is the only scattering process which classically conserves energy, while also conserving the quasimomentum. We therefore expect that scattering into states with momentum $p > |\hbar K/2|$ ought to be strongly suppressed even under the fully quantum time evolution. We explore this simplified picture in Sec. III.

III. REDUCTION TO AN EFFECTIVE TWO-STATE SYSTEM

A. Simplification

We may test the conjecture that population transfer into states with $k < -1$ or $k > 0$ is strongly suppressed by computing the full time evolution of the system numerically. The results of such calculations on an exhaustive basis of momentum states are displayed in Fig. 2. Over the 13 basis states displayed, we can clearly see that, though population transfer into higher-order modes does occur, the oscillation of population between the $k = -1$ and the $k = 0$ states is the dominant process in the system. We therefore expect that a representation of the system in a truncated momentum basis composed of only these two states ought to capture the essential dynamics and explore this simplified two-state model below.

B. Two-state model analytics

We may represent the Hamiltonian, (3), in the $\beta = 1/2$ subspace using the two-state momentum basis

$$|k = 0\rangle = \begin{pmatrix} 1 \\ 0 \end{pmatrix}, \tag{6a}$$

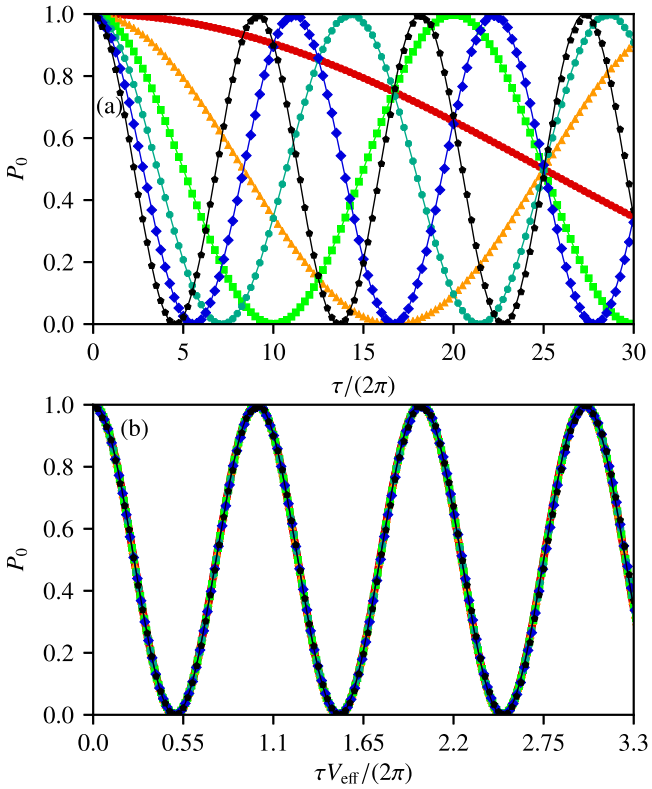

FIG. 3. (a) Plot of P_0, the population in the $|k=0\rangle$ state, versus $\tau V_{\rm eff}/(2\pi)$, as calculated on a basis of 2048 momentum states using a split-step Fourier method (filled symbols). Solid lines correspond to the analytic solution for P_0 in the two-state basis, as given by Eq. (8a). Each set of markers corresponds to a fixed value of the effective lattice depth, ranging from the slowest-oscillating curve at $V_{\rm eff}=0.01$ to the fastest-oscillating one at $V_{\rm eff}=0.11$, in steps of 0.02. (b) Reproduction of (a), with the dimensionless time axis scaled by $V_{\rm eff}$ to reveal a universal curve both in the analytics and in the numerical simulations. The data have been extended to span the full range of the horizontal axis.

$$|k=-1\rangle=\begin{pmatrix}0\\1\end{pmatrix}, \tag{6b}$$

yielding

$$H^{2\times2}_{\rm Latt}=\begin{pmatrix}1/8 & -V_{\rm eff}/2\\ -V_{\rm eff}/2 & 1/8\end{pmatrix}. \tag{7}$$

We recognize Eq. (7) as a Rabi matrix with zero detuning, the eigenvectors and eigenvalues of which are well known [34] and can be used to straightforwardly determine the time evolution of the population in the $|k=0\rangle$ and $|k=-1\rangle$ states, respectively,

$$P_0=\cos^2(V_{\rm eff}\tau/2), \tag{8a}$$

$$P_{-1}=\sin^2(V_{\rm eff}\tau/2), \tag{8b}$$

as outlined in Appendix A. This analytic result is compared to our exact numerics in Figs. 2 and 3, both of which show excellent agreement for a wide range of experimentally relevant values of the effective lattice depth $V_{\rm eff}$. We note, in particular, that the form of Eqs. (8a) and (8b) is such that there is an exact universality between τ and $V_{\rm eff}$, which is elucidated in Fig. 3(b), where all population curves fall on top of each other.

IV. FINITE-TEMPERATURE RESPONSE

A. Other values of β

In the following section we consider the effect of evolving initial states with quasimomentum other than $\beta=1/2$ in order to gain insight into the dynamics of a finite-temperature gas. Numerically, this is achieved by computing the evolution of an initial state $|k+\beta\rangle$ under the time evolution operator, (5). We make the assumption from the outset that the initial momentum distribution of the gas (centered at $\beta=1/2$) spans less than half of each of the $k=0$ and $k=-1$ Brillouin zones for a static grating (or falls within the $k=0$ Brillouin zone with a momentum distribution centered on $\beta=0$ for a walking grating). Our results in this low-temperature regime are displayed in Fig. 4, which indicates a $k=0$ Brillouin zone with high-amplitude but low-frequency oscillations in the population of the zeroth diffraction order centered around $|\beta|=1/2$ and low-amplitude but rapidly oscillating solutions as β is detuned from this value. We may also use our simplified semiclassical model in Sec. III to derive an approximate analytic result for the same calculation, in which the quasimomentum β is encoded as a detuning to be included in our initial Rabi model of Eq. (7). These additions yield the 2×2 Hamiltonian matrix

$$H^{2\times2}_{\rm Latt}(\beta)=\begin{pmatrix}\beta^2/2 & -V_{\rm eff}/2\\ -V_{\rm eff}/2 & (1-2\beta+\beta^2)/2\end{pmatrix}, \tag{9}$$

in which β is now a free parameter. The time evolution of the zeroth-diffraction-order population governed by this matrix can be found using the approach given in Appendix B, thus

$$P_0(\beta)=1-\frac{V_{\rm eff}^2}{(\beta-1/2)^2+V_{\rm eff}^2}\sin^2\left(\sqrt{(\beta-1/2)^2+V_{\rm eff}^2}\,\frac{\tau}{2}\right), \tag{10}$$

which is similar to the result reported in [15] for a zero-temperature gas and agrees excellently with the exact numerics for values of the quasimomentum close to $\beta=1/2$ as shown in Fig. 4. For β close to 0, however, the effective driving is equally off-resonant from both the $|k=1\rangle$ and the $|k=-1\rangle$ states, meaning that our analytic Rabi model consisting of only the $|0\rangle$ and $|-1\rangle$ states underestimates the population diffracted out of the $|0\rangle$ state. Nonetheless, we expect that thermal averaging of this result should produce an accurate description of the full finite-temperature response if the initial momentum distribution is sufficiently narrow.

B. Finite-temperature analysis

To find the finite-temperature response of the system we weight the contribution of Eq. (10) for each individual quasimomentum subspace according to the Maxwell-Boltzmann distribution,

$$D_{k=0}(\beta,w)=\frac{1}{w\sqrt{2\pi}}\exp\left(\frac{-(\beta-1/2)^2}{2w^2}\right), \tag{11}$$

where the dimensionful temperature is given by $\mathcal{T}_w=\hbar^2K^2w^2/Mk_B$ [35]. Mathematically this corresponds to the

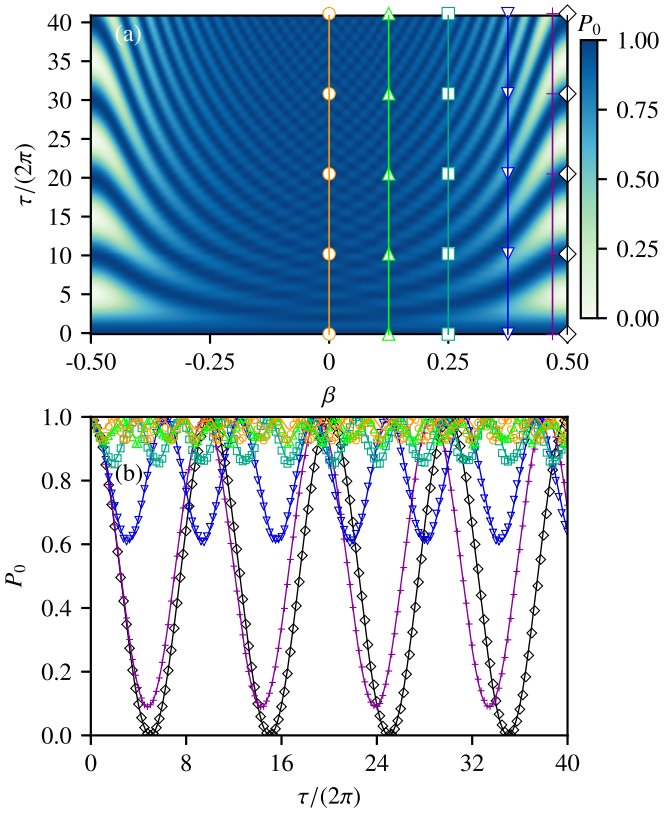

FIG. 4. (a) False-color plot of the time evolution of P_0 as computed on a basis of 2048 momentum states for values of the dimensionless quasimomentum β [see Eqs. (4b) and (4c)] ranging from $\beta = -0.5$ to $\beta = 0.5$ in steps of $\beta = 0.000\,25$ (4001 quasimomentum values). We chose the relatively large lattice depth of $V_{\text{eff}} = 0.1$ so that the different dynamical behaviors are made clear for the chosen evolution time $\tau/(2\pi) = 40$. (b) Slices taken through the quasimomentum distribution parallel to the time axis for $\beta = 0$, 0.0625, and 0.125, then increasing in increments of $\beta = 0.125$ up to a maximum of $\beta = 0.5$, enclosing the full range of dynamics in the $k = 0$ subspace. Each vertical set of markers in (a) corresponds to the position in the quasimomentum distribution of the slices in (b), where the solid lines represent our analytic solution for each β subspace [Eq. (10)].

integral

$$P_0(w) = \int_0^1 D_{k=0}(\beta, w) P_0(\beta) d\beta. \tag{12}$$

Inserting Eqs. (11) and (10), we have

$$P_0(\rho) = \frac{1}{\sqrt{2\pi}\rho} \int_{-1/2}^{1/2} \exp\left(\frac{-\gamma^2}{2\rho^2}\right) \times \left[1 - \frac{1}{\gamma^2+1} \sin^2\left(\frac{\sqrt{\gamma^2+1}}{2}\phi\right)\right] d\gamma, \tag{13}$$

where we have introduced $\gamma = (\beta - 1/2)/V_{\text{eff}}$, $\phi = V_{\text{eff}}\tau$, and $\rho = w/V_{\text{eff}}$ for simplicity. The exponential and trigonometric terms can be power expanded, and the integral, (13), solved term by term, giving

$$P_0(\rho) = 1 - \sum_{s=0}^{\infty} \sum_{q=0}^{s} u_s(\phi) M_{s,q} v_q(\rho), \tag{14}$$

where $u_s(\phi) = (-\phi^2)^{s+1} s!/[2(s+1)]!$, $M_{s,q} = -(2q)!/[2(q!)^2(s-q)!]$, and $v_q(\rho) = (\rho^2/2)^q$ (see Appendix C). Equation (14) can in principle be solved numerically by recursively populating the elements of a sufficiently large pair of $u(\phi)$, $v(\rho)$ vectors and M matrix, though the elements of the vectors will grow with s and q, respectively, unless ϕ and ρ are sufficiently small, and this condition is only satisfied for certain experimentally relevant regimes. Nonetheless, Eq. (14) yields some insight when expressed as a sum over derivatives of sinc functions (see Appendix D):

$$P_0(\rho) = 1 - \sum_{q=0}^{\infty} \left(\frac{\rho}{2}\right)^{2q} \frac{(2q)!}{q!^2} \times \left\{\left(\frac{\phi}{2}\right)^{2(q+1)} \left[\left(\frac{2}{\phi}\right)\frac{d}{d(\phi/2)}\right]^q \left[\frac{\sin^2(\phi/2)}{(\phi/2)^2}\right]\right\}. \tag{15}$$

With $q = 0$, Eq. (15) reduces to the zero-temperature result of Eq. (8a); as such we should expect the finite-temperature behavior of the system to be captured in terms with $q > 0$. Though the full sum over q is always convergent, the presence of the $(\phi/2)^{2(q+1)}$ term guarantees that all individual terms with $q \geqslant 1$ diverge, meaning that a preferred truncation of the sum is not obvious.

However, given the well-behaved nature of the integrand, Eq. (13) can be straightforwardly integrated numerically, for instance, using the trapezium rule. We compare this numerical integration to our full finite-temperature numerics in Fig. 5, which shows excellent agreement across a large range of initial momentum widths in the weak lattice regime [Figs. 5(a) and 5(b)] and for $V_{\text{eff}} = 0.1$ in the relatively stronger lattice regime [Fig. 5(d)]. However, for $V_{\text{eff}} = 0.5$ [Fig. 5(c)] the agreement is relatively poor, as in this regime the semiclassically motivated two-state model is no longer valid. We therefore expect that numerically fitting Eq. (13) to experimental data, with $\phi = V_{\text{eff}}\tau$ and $\rho = w/V_{\text{eff}}$ as free parameters, would give an accurate value of the effective lattice depth, if the time τ is known to a high precision and the lattice depth is sufficiently small.

Further, we note that using standard integral results, we may also extract the steady-state solution to Eq. (13) as $\phi \to \infty$,

$$P_{0,\phi\to\infty}(\rho) = \frac{1}{2\rho}\sqrt{\frac{\pi}{2}} \exp\left(\frac{1}{2\rho^2}\right) \text{Erfc}\left(\frac{1}{\sqrt{2}\rho}\right), \tag{16}$$

which depends only on $\rho = w/V_{\text{eff}}$. Here, Erfc is the complementary error function [36].[4] In essence, by measuring the steady-state population experimentally, and numerically

[4]When evaluating Eq. (16) for physically relevant values of $\rho = w/V_{\text{eff}}$, the exponential term becomes large as the error function takes a correspondingly smaller value such that $P_{0,\phi\to\infty}(\rho)$ remains bounded between 0 and 1. This complication can present a problem for numerical evaluation using standard numerical routines. In

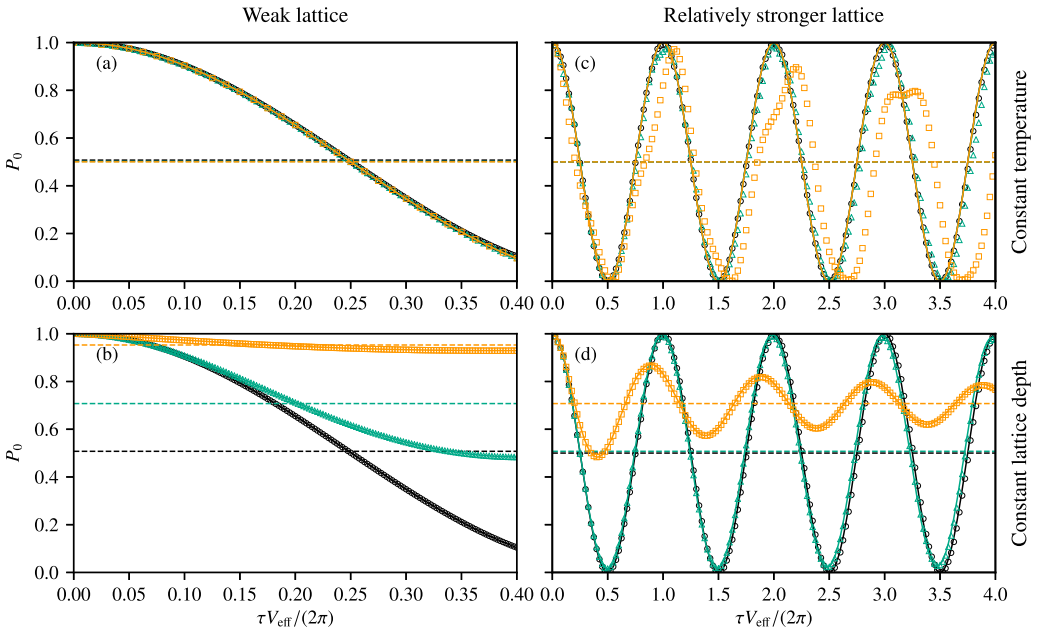

FIG. 5. Plot of the finite-temperature response of P_0 vs $\tau V_{\rm eff}/(2\pi)$, where $V_{\rm eff}$ is the dimensionless lattice depth [see Eq. (5)], as calculated for an ensemble of 4001 particles each evolved in a basis of 2048 momentum states (open symbols). The left column [(a), (b)] corresponds to the weak lattice regime, and the right column [(c), (d)] to the relatively stronger lattice regime. The top row of plots [(a), (c)] shows the finite-temperature response of P_0 at a temperature of $w = 0.001\,25$ for a selection of different lattice depths, $V_{\rm eff} = 0.01$, 0.02, and 0.05 (all curves fall on top of each other) in the weak regime (a) and $V_{\rm eff} = 0.1$, 0.2, and 0.5 (lower, middle, and uppermost curves) in the relatively stronger regime (b). In the bottom row [(b), (d)], each set of curves and markers corresponds to the response of P_0 at a different temperature ($w = 0.001\,25$, 0.0125, and 0.125; lower, middle, and uppermost curves, respectively), where the effective lattice depth is kept constant at $V_{\rm eff} = 0.1$ in the stronger-lattice case and $V_{\rm eff} = 0.01$ in the weak-lattice case. In all panels, solid lines represent the result yielded by numerically integrating Eq. (13). Dashed horizontal lines correspond to the result of the steady-state solution of Eq. (16) for each set of parameters.

fitting Eq. (16), $\rho = w/V_{\rm eff}$ can be straightforwardly determined and substituted into Eq. (13), leaving a fit for only one parameter, $\phi = V_{\rm eff}\tau$. The steady-state population can in principle be found either by allowing the atomic gas to evolve in the lattice for a sufficiently long time or by taking the average value of P_0 in time over an appropriate number of oscillations; how practical this is will depend on the typical lifetimes of any given experiment, although the possibility always remains to fit Eq. (13) to the available data. In fact, this improved fitting approach not only allows $\phi = V_{\rm eff}\tau$, and therefore the effective lattice depth $V_{\rm eff}$, to be determined more accurately, but also allows the initial effective temperature to be determined via $w = \rho V_{\rm eff}$ from the same experimental data set.

V. CONCLUSIONS

We have presented a simplified model system yielding an analytic zero-temperature formula for the evolution of the zeroth-diffraction-order population and demonstrated the validity of this approach across a wide range of lattice depths. We have extended this model to incorporate finite-temperature effects and discussed where they originate mathematically. We have shown that there is excellent agreement between this analytic model and exact numerical calculations if the lattice depth is sufficiently small. We have also determined steady-state solutions, which may be useful for determining both the lattice depth and the initial temperature of a gas from a common experimental data set. Such a data set would consist of multiple experimental runs of increasing duration carried out on the same atomic initial condition followed by population measurements. With regard to potential experimental implementations, we note that the phase velocity of a walking optical lattice can be calibrated extremely precisely via a system of acousto-optic modulators calibrated by a known frequency difference. We further note that such elements are quite commonly in place in optical lattice setups, in which case one would expect an adaptation to include the necessary functionality to implement the dynamics described in this paper to be relatively straightforward. If this is not the case, however, the alternative is to impart a specified momentum to an initially stationary BEC, although it is unlikely that this can be achieved to the same level of precision.

Finally, we note that in the system we have studied, unit fringe visibility is in principle achievable (i.e., complete population transfer between the two lowest bands of the optical lattice, as shown in Figs. 3 and 5). This is not possible, even at zero temperature, for the pulsed configuration initially studied by Herold *et al.* [21–23], and in the case of observing Rabi oscillations in the manner of Ovchinnikov *et al.* [19] (i.e., with a static standing-wave optical lattice and an initially static

practice, we numerically implement Eq. (16) exclusively in terms of rational numbers in Mathematica, before requesting a numerical evaluation to a specified precision.

atomic sample) the fringe visibility becomes vanishingly small in the case of weak lattices. On this criterion alone, we believe the system dynamics we have described in this paper offer significant advantages as a potential means of accurate determination of weak optical lattice depths, which can be of great utility, for example, in the accurate determination of transition matrix elements [21,22].

ACKNOWLEDGMENTS

B.T.B., I.G.H., and S.A.G. thank the Leverhulme Trust research program, Grant No. RP2013-k-009, SPOCK: Scientific Properties of Complex Knots, for support. We would also like to acknowledge helpful discussions with Andrew R. MacKellar.

APPENDIX A: DERIVATION OF THE TWO-STATE MODEL

To calculate the time evolution of the population in the zeroth diffraction order, we construct the time evolution operator in the momentum basis from the Hamiltonian of Eq. (7), reproduced here for convenience:

$$H_{\mathrm{Latt}}^{2\times2} = \begin{pmatrix} 1/8 & -V_{\mathrm{eff}}/2 \\ -V_{\mathrm{eff}}/2 & 1/8 \end{pmatrix}. \tag{A1}$$

The diagonal terms simply represent an energy shift that can be transformed away, after which the eigenvalues of Eq. (7) can simply be read from the off-diagonal: $E_\pm = \pm V_{\mathrm{eff}}/2$. We may now solve the eigenvalue equation:

$$\begin{pmatrix} 0 & -V_{\mathrm{eff}}/2 \\ -V_{\mathrm{eff}}/2 & 0 \end{pmatrix}\begin{pmatrix} v_1^\pm \\ v_0^\pm \end{pmatrix} = \pm V_{\mathrm{eff}}/2 \begin{pmatrix} v_1^\pm \\ v_0^\pm \end{pmatrix}. \tag{A2}$$

Equation (A2) leads directly to $-v_1^\pm = \pm v_0^\pm$, yielding eigenvectors

$$|E_+\rangle = \frac{1}{\sqrt{2}}\begin{pmatrix} 1 \\ -1 \end{pmatrix}, \quad |E_-\rangle = \frac{1}{\sqrt{2}}\begin{pmatrix} 1 \\ 1 \end{pmatrix}. \tag{A3}$$

We may now construct our initial condition in the energy basis, in which the matrix representation of the time evolution operator

$$\hat{U}(\tau) = \exp(-i\hat{H}_{\mathrm{Latt}}\tau) \tag{A4}$$

is diagonal:

$$|\psi(\tau=0)\rangle = |k=0\rangle = \frac{1}{\sqrt{2}}(|E_+\rangle + |E_-\rangle). \tag{A5}$$

The time evolution of the population in the zeroth diffraction order is given by

$$\begin{aligned} P_0 &= \left|\frac{1}{2}(\langle E_+| + \langle E_-|)\hat{U}(\tau)(|E_+\rangle + |E_-\rangle)\right|^2 \\ &= \frac{1}{4}\left|e^{-iE_+\tau} + e^{-iE_-\tau}\right|^2 \\ &= \frac{1}{4}\left|e^{-iV_{\mathrm{eff}}\tau/2} + e^{iV_{\mathrm{eff}}\tau/2}\right|^2 \\ &= \cos^2(V_{\mathrm{eff}}\tau/2), \end{aligned} \tag{A6}$$

which corresponds to Eq. (8a).

APPENDIX B: DERIVATION OF THE β-DEPENDENT TWO-STATE MODEL

To calculate the time-evolved population for a given quasimomentum subspace, we follow the same procedure as in Appendix A. Equation (9), reproduced here for convenience,

$$H_{\mathrm{Latt}}^{2\times2}(\beta) = \begin{pmatrix} \beta^2/2 & -V_{\mathrm{eff}}/2 \\ -V_{\mathrm{eff}}/2 & (1-2\beta+\beta^2)/2 \end{pmatrix},$$

is nothing other than a Rabi matrix, the eigenvalues of which are $E_\pm = [(1/2-\beta+\beta^2) \pm \sqrt{(\beta-1/2)^2 + V_{\mathrm{eff}}^2}]/2$, and the corresponding eigenvectors

$$\begin{aligned} |E_+\rangle &= \begin{pmatrix} \cos(\alpha/2) \\ \sin(\alpha/2) \end{pmatrix} = \frac{1}{\sqrt{2}}\big[\sqrt{1+\cos(\alpha)}|k=0\rangle \\ &\quad + \sqrt{1-\cos(\alpha)}|k=-1\rangle\big], \end{aligned} \tag{B1a}$$

$$\begin{aligned} |E_+\rangle &= \begin{pmatrix} -\sin(\alpha/2) \\ \cos(\alpha/2) \end{pmatrix} = -\frac{1}{\sqrt{2}}\big[\sqrt{1-\cos(\alpha)}|k=0\rangle \\ &\quad - \sqrt{1+\cos(\alpha)}|k=-1\rangle\big], \end{aligned} \tag{B1b}$$

where $\cos(\alpha) = (\beta-1/2)/\sqrt{(\beta-1/2)^2+V_{\mathrm{eff}}^2}$. This leads directly to

$$\begin{aligned} |\psi(\tau=0)\rangle &= |k=0\rangle = \cos(\alpha/2)|E_+\rangle - \sin(\alpha/2)|E_-\rangle \\ &= \frac{1}{\sqrt{2}}[\sqrt{1+\cos(\alpha)}|E_+\rangle - \sqrt{1-\cos(\alpha)}|E_-\rangle]. \end{aligned}$$

We may now simply calculate the time-evolved state from the action of the time evolution operator

$$\hat{U}(\tau,\beta) = \exp\left(-i\hat{H}(\beta)_{\mathrm{Latt}}\tau\right)$$

on this initial state thus:

$$\begin{aligned} |\psi(\tau,\beta)\rangle &= \exp(-i\hat{H}(\beta)_{\mathrm{Latt}}\tau)|k=0\rangle \\ &= \frac{1}{\sqrt{2}}\big[\sqrt{1+c}\,e^{-iE_+\tau}|E_+\rangle + \sqrt{1-c}\,e^{-iE_-\tau}|E_-\rangle\big]. \end{aligned}$$

Here we have introduced $c \equiv \cos(\alpha)$. The time-evolved population in the zeroth diffraction order for a given β subspace is then given by

$$\begin{aligned} p_0(\tau,\beta) &= |\langle k=0|\psi(\tau,\beta)\rangle|^2 \\ &= \frac{1}{4}\left|(1+c)\,e^{-iE_+\tau} + (1-c)\,e^{-iE_-\tau}\right|^2 \\ &= \frac{1}{4}\Big|e^{E_+\tau/2}e^{E_-\tau/2}\big[(1+c)\,e^{-i[E_+-E_-]\tau/2} \\ &\quad + \ (1-c)\,e^{i[E_+-E_-]\tau/2}\big]\Big|^2 \\ &= \cos^2([E_+-E_-]\tau/2) + c^2\sin^2([E_+-E_-]\tau/2) \\ &= 1 + (c^2-1)\sin^2([E_+-E_-]\tau/2) \\ &= 1 - \frac{V_{\mathrm{eff}}^2}{(\beta-1/2)^2+V_{\mathrm{eff}}^2}\sin^2\left(\sqrt{(\beta-1)^2+V_{\mathrm{eff}}^2}\,\tau/2\right), \end{aligned} \tag{B2}$$

which corresponds to Eq. (10).

APPENDIX C: DERIVATION OF THE FINITE-TEMPERATURE MATRIX EQUATION

To derive the matrix equation for the finite-temperature response of the zeroth-diffraction-order population, we begin from Eq. (12), into which we insert Eqs. (11) and (10), yielding

$$P_0(w) = 1 - \frac{1}{\sqrt{2\pi}\,w}\int_{-\infty}^{\infty} d\alpha\,\frac{V_{\rm eff}^2}{\alpha^2+V_{\rm eff}^2}\exp\left(\frac{-\alpha^2}{2w^2}\right)\sin^2\left(\sqrt{\alpha^2+V_{\rm eff}^2}\,\frac{\tau}{2}\right) = 1 - P_{-1}(w), \tag{C1}$$

where we have introduced $\alpha \equiv (\beta - 1/2)$. For simplicity, we now refer to $P_{-1}(w)$, the population in the $|k=-1\rangle$ state. The sinusoidal term can be rewritten using $\sin^2(\theta) = [1-\cos(2\theta)]/2$ thus:

$$P_{-1}(w) = \frac{V_{\rm eff}^2}{\sqrt{2\pi}\,w}\int_0^{\infty} d\alpha\,\frac{1}{\alpha^2+V_{\rm eff}^2}\exp\left(\frac{-\alpha^2}{2w^2}\right)\left[1-\cos\left(\sqrt{\alpha^2+V_{\rm eff}^2}\,\tau\right)\right], \tag{C2}$$

where we have used the fact that the integrand is an even function. The term in $\cos(\sqrt{\alpha^2+V_{\rm eff}^2}\,\tau)$ can then be power expanded, leading to

$$\begin{aligned} P_{-1}(w) &= \frac{V_{\rm eff}^2}{\sqrt{2\pi}\,w}\int_0^{\infty} d\alpha\,\frac{-1}{\alpha^2+V_{\rm eff}^2}\exp\left(\frac{-\alpha^2}{2w^2}\right)\sum_{s=1}^{\infty}\frac{(-1)^s\left(\alpha^2+V_{\rm eff}^2\right)^s\tau^{2s}}{(2s)!} \\ &= \frac{V_{\rm eff}^2}{\sqrt{2\pi}\,w}\sum_{s=0}^{\infty}\frac{(-1)^s\tau^{2(s+1)}}{(2[s+1])!}\int_0^{\infty} d\alpha\exp\left(\frac{-\alpha^2}{2w^2}\right)\left(\alpha^2+V_{\rm eff}^2\right)^s, \end{aligned}$$

such that the square root in the argument no longer appears, and the $(\alpha^2+V_{\rm eff}^2)^s$ term can be binomially expanded thus:

$$P_{-1}(w) = \frac{V_{\rm eff}^2}{\sqrt{2\pi}\,w}\sum_{s=0}^{\infty}\frac{(-1)^s\tau^{2(s+1)}s!}{(2[s+1])!}\sum_{q=0}^{s}\frac{V^{2(s-q)}}{q!(s-q)!}\int_0^{\infty} d\alpha\,\alpha^{2q}\exp\left(\frac{-\alpha^2}{2w^2}\right). \tag{C3}$$

Further, introducing $\xi \equiv \alpha^2/(2w^2)$, the remaining integral can be rewritten as

$$\begin{aligned} \int_0^{\infty} d\alpha\,\alpha^{2q}\exp\left(\frac{-\alpha^2}{2w^2}\right) &= w^{2q+1}2^{q-1/2}\int_0^{\infty} d\xi\,\exp(-\xi)\xi^{q-1/2} \\ &= w^{2q+1}2^{q-1/2}\Gamma(q+1/2), \end{aligned}$$

which, when substituted into Eq. (C3), leads to

$$P_{-1}(w) = \frac{1}{2\sqrt{\pi}}\sum_{s=0}^{\infty}\frac{(-1)^s(V_{\rm eff}\tau)^{2(s+1)}s!}{(2[s+1])!}\sum_{q=0}^{s}\frac{1}{q!(s-q)!}\left(\frac{2w^2}{V_{\rm eff}^2}\right)^q\Gamma(q+1/2). \tag{C4}$$

Finally, noting that $\Gamma(s+1/2) = (2s)!\sqrt{\pi}/(2^{2s}s!)$, Eq. (C4) can be rewritten as

$$P_{-1}(w) = \sum_{s=0}^{\infty}\sum_{q=0}^{s}\frac{\left(-V_{\rm eff}^2\tau^2\right)^{s+1}s!}{(2[s+1])!}\frac{\left(-\frac{1}{2}\right)(2q)!}{(q!)^2(s-q)!}\left(\frac{w^2}{2V_{\rm eff}^2}\right)^q = u_s(V_{\rm eff}\tau)M_{s,q}v_q(w/V_{\rm eff}) \tag{C5}$$

or, equivalently, with $\phi = V_{\rm eff}\tau$ and $\rho = w/V_{\rm eff}$,

$$P_0(\rho) = 1 - P_{-1}(\rho) = 1 - \sum_{s=0}^{\infty}\sum_{q=0}^{s}u_s(\phi)M_{s,q}v_q(\rho),$$

which corresponds to Eq. (14).

APPENDIX D: EXPRESSION OF EQ. (14) IN TERMS OF sinc FUNCTIONS

Equation (C5) can be rewritten as

$$P_{-1}(\rho) = \sum_{q=0}^{\infty}\left(\frac{\rho^2}{2}\right)^q\frac{(2q)!}{q!^2}\left\{\left(\frac{-1}{2}\right)\sum_{s=q}^{\infty}\frac{s!}{(2[s+1])!(s-q)!}(-\phi^2)^{s+1}\right\},$$

where we have used $\phi = V_{\rm eff}t$ and $\rho = w/V_{\rm eff}$. We now introduce $\tau = \phi^2$ and reindex the sum in s, yielding

$$P_{-1}(\rho) = \sum_{q=0}^{\infty}\left(\frac{\rho^2}{2}\right)^q\frac{(2q)!}{q!^2}\left\{\left(\frac{-1}{2}\right)\sum_{s=q+1}^{\infty}\frac{(s-1)!}{(2s)!(s-1-q)!}(-1)^s\tau^s\right\}.$$

Expanding the factorial terms in s and rearranging in τ,

$$P_{-1}(\rho)=\sum_{q=0}^{\infty}\left(\frac{\rho^2}{2}\right)^q\frac{(2q)!}{q!^2}\left\{\tau^{q+1}\left(\frac{-1}{2}\right)\sum_{s=1}^{\infty}\frac{(s-1)(s-2)\ldots(s-q)}{(2s)!}(-1)^s\tau^{s-q-1}\right\},$$

which we recognize can be expressed as a derivative in q thus:

$$P_{-1}(\rho)=\sum_{q=0}^{\infty}\left(\frac{\rho^2}{2}\right)^q\frac{(2q)!}{q!^2}\left\{\tau^{q+1}\left(\frac{-1}{2}\right)\frac{d^q}{d\tau^q}\sum_{s=1}^{\infty}\frac{(-1)^s\tau^{s-1}}{(2s)!}\right\}. \tag{D1}$$

Equation (D1) can be rewritten,

$$P_{-1}(\rho)=\sum_{q=0}^{\infty}\left(\frac{\rho^2}{2}\right)^q\frac{(2q)!}{q!^2}\left\{\tau^{q+1}\frac{d^q}{d\tau^q}\left(\frac{1}{\tau}\left[-\frac{1}{2}\sum_{s=1}^{\infty}\frac{(-1)^s\tau^{s-1}}{(2s)!}\right]\right)\right\},$$

such that the sum in s can now be recognized as a sinusoidal term, yielding

$$P_{-1}(\rho)=\sum_{q=0}^{\infty}\left(\frac{\rho^2}{2}\right)^q\frac{(2q)!}{q!^2}\left\{\tau^{q+1}\frac{d^q}{d\tau^q}\left(\frac{1}{\tau}\left[\frac{\sin^2(\sqrt{\tau}/2)}{\tau}\right]\right)\right\}.$$

Reintroducing ϕ leads to

$$\begin{aligned}P_{-1}(\rho)&=\sum_{q=0}^{\infty}\left(\frac{\rho^2}{2}\right)^q\frac{(2q)!}{q!^2}\left\{\phi^{2(q+1)}\left(\frac{1}{2\phi}\frac{d}{d\phi}\right)^q\left[\frac{\sin^2(\phi/2)}{\phi^2}\right]\right\}=\frac{1}{2}\sum_{q=0}^{\infty}\left(\frac{\rho^2}{2}\right)^q\frac{(2q)!}{q!^2}\left\{\left(\frac{\phi^2}{2}\right)^{q+1}\left(\frac{1}{\phi}\frac{d}{d\phi}\right)^q\left[\frac{\sin^2(\phi/2)}{\phi^2}\right]\right\}\\&=\frac{1}{2}\sum_{q=0}^{\infty}\left(\frac{\rho^2}{2}\right)^q\frac{(2q)!}{q!^2}\left\{\left(\frac{\phi^2}{2}\right)^{q+1}\frac{1}{2^{2q}}\left[\left(\frac{2}{\phi}\right)\frac{d}{d(\phi/2)}\right]^q\left[\frac{\sin^2(\phi/2)}{\phi^2}\right]\right\}.\end{aligned}$$

Equivalently,

$$P_0(\rho)=1-P_1(\rho)=1-\sum_{q=0}^{\infty}\left(\frac{\rho}{2}\right)^{2q}\frac{(2q)!}{q!^2}\left\{\left(\frac{\phi}{2}\right)^{2(q+1)}\left[\left(\frac{2}{\phi}\right)\frac{d}{d(\phi/2)}\right]^q\left[\frac{\sin^2(\phi/2)}{(\phi/2)^2}\right]\right\},$$

which corresponds to Eq. (15).

[1] O. Morsch and M. Oberthaler, Dynamics of Bose-Einstein condensates in optical lattices, Rev. Mod. Phys. **78**, 179 (2006).

[2] J. Mitroy, M. S. Safronova, and C. W. Clark, Theory and applications of atomic and ionic polarizabilities, J. Phys. B **43**, 202001 (2010).

[3] B. Arora, M. S. Safronova, and C. W. Clark, Tune-out wavelengths of alkali-metal atoms and their applications, Phys. Rev. A **84**, 043401 (2011).

[4] B. M. Henson, R. I. Khakimov, R. G. Dall, K. G. H. Baldwin, L.-Y. Tang, and A. G. Truscott, Precision Measurement for Metastable Helium Atoms of the 413 nm Tune-Out Wavelength at Which the Atomic Polarizability Vanishes, Phys. Rev. Lett. **115**, 043004 (2015).

[5] R. H. Leonard, A. J. Fallon, C. A. Sackett, and M. S. Safronova, High-precision measurements of the ^{87}Rb D-line tune-out wavelength, Phys. Rev. A **92**, 052501 (2015).

[6] L. W. Clark, L.-C. Ha, C.-Y. Xu, and C. Chin, Quantum Dynamics with Spatiotemporal Control of Interactions in a Stable Bose-Einstein Condensate, Phys. Rev. Lett. **115**, 155301 (2015).

[7] M. S. Safronova, M. G. Kozlov, and C. W. Clark, Precision Calculation of Blackbody Radiation Shifts for Optical Frequency Metrology, Phys. Rev. Lett. **107**, 143006 (2011).

[8] J. A. Sherman, N. D. Lemke, N. Hinkley, M. Pizzocaro, R. W. Fox, A. D. Ludlow, and C. W. Oates, High-Accuracy Measurement of Atomic Polarizability in an Optical Lattice Clock, Phys. Rev. Lett. **108**, 153002 (2012).

[9] D. J. Whiting, J. Keaveney, C. S. Adams, and I. G. Hughes, Direct measurement of excited-state dipole matrix elements using electromagnetically induced transparency in the hyperfine Paschen-Back regime, Phys. Rev. A **93**, 043854 (2016).

[10] A. D. Cronin, J. Schmiedmayer, and D. E. Pritchard, Optics and interferometry with atoms and molecules, Rev. Mod. Phys. **81**, 1051 (2009).

[11] A. Miffre, M. Jacquey, M. Büchner, G. Trénec, and J. Vigué, Atom interferometry, Phys. Scr. **74**, C15 (2006).

[12] I. Bloch, J. Dalibard, and W. Zwerger, Many-body physics with ultracold gases, Rev. Mod. Phys. **80**, 885 (2008).

[13] G.-B. Jo, J. Guzman, C. K. Thomas, P. Hosur, A. Vishwanath, and D. M. Stamper-Kurn, Ultracold Atoms in a Tunable Optical Kagome Lattice, Phys. Rev. Lett. **108**, 045305 (2012).

[14] S. B. Cahn, A. Kumarakrishnan, U. Shim, T. Sleator, P. R. Berman, and B. Dubetsky, Time-Domain De Broglie Wave Interferometry, Phys. Rev. Lett. **79**, 784 (1997).

[15] B. Gadway, D. Pertot, R. Reimann, M. G. Cohen, and D. Schneble, Analysis of Kapitza-Dirac diffraction patterns beyond the Raman-Nath regime, Opt. Express **17**, 19173 (2009).

[16] G. Birkl, M. Gatzke, I. H. Deutsch, S. L. Rolston, and W. D. Phillips, Bragg Scattering from Atoms in Optical Lattices, Phys. Rev. Lett. **75**, 2823 (1995).

[17] P. Cheiney, C. M. Fabre, F. Vermersch, G. L. Gattobigio, R. Mathevet, T. Lahaye, and D. Guéry-Odelin, Matter-wave scattering on an amplitude-modulated optical lattice, Phys. Rev. A **87**, 013623 (2013).

[18] S. Friebel, C. D'Andrea, J. Walz, M. Weitz, and T. W. Hänsch, CO_2-laser optical lattice with cold rubidium atoms, Phys. Rev. A **57**, R20 (1998).

[19] Yu. B. Ovchinnikov, J. H. Müller, M. R. Doery, E. J. D. Vredenbregt, K. Helmerson, S. L. Rolston, and W. D. Phillips, Diffraction of a Released Bose-Einstein Condensate by a Pulsed Standing Light Wave, Phys. Rev. Lett. **83**, 284 (1999).

[20] C. Cabrera-Gutiérrez, E. Michon, V. Brunaud, T. Kawalec, A. Fortun, M. Arnal, J. Billy, and D. Guéry-Odelin, Robust calibration of an optical-lattice depth based on a phase shift, Phys. Rev. A **97**, 043617 (2018).

[21] C. D. Herold, V. D. Vaidya, X. Li, S. L. Rolston, J. V. Porto, and M. S. Safronova, Precision Measurement of Transition Matrix Elements via Light Shift Cancellation, Phys. Rev. Lett. **109**, 243003 (2012).

[22] W. Kao, Y. Tang, N. Q. Burdick, and B. L. Lev, Anisotropic dependence of tune-out wavelength near Dy 741-nm transition, Opt. Express **25**, 3411 (2017).

[23] B. T. Beswick, I. G. Hughes, and S. A. Gardiner, Lattice-depth measurement using multipulse atom diffraction in and beyond the weakly diffracting limit, Phys. Rev. A **99**, 013614 (2019).

[24] M. Bienert, F. Haug, W. P. Schleich, and M. G. Raizen, Kicked rotor in Wigner phase space, Fortschr. Phys. **51**, 474 (2003).

[25] B. T. Beswick, I. G. Hughes, S. A. Gardiner, H. P. A. G. Astier, M. F. Andersen, and B. Daszuta, ϵ-pseudoclassical model for quantum resonances in a cold dilute atomic gas periodically driven by finite-duration standing-wave laser pulses, Phys. Rev. A **94**, 063604 (2016).

[26] N. W. Ashcroft and N. D. Mermin, *Solid State Physics* (Saunders College, Philadelphia, 1976).

[27] R. Bach, K. Burnett, M. B. d'Arcy, and S. A. Gardiner, Quantum-mechanical cumulant dynamics near stable periodic orbits in phase space: Application to the classical-like dynamics of quantum accelerator modes, Phys. Rev. A **71**, 033417 (2005).

[28] B. Daszuta and M. F. Andersen, Atom interferometry using δ-kicked and finite-duration pulse sequences, Phys. Rev. A **86**, 043604 (2012).

[29] P. J. Martin, B. G. Oldaker, A. H. Miklich, and D. E. Pritchard, Bragg Scattering of Atoms from a Standing Light Wave, Phys. Rev. Lett. **60**, 515 (1988).

[30] D. M. Giltner, R. W. McGowan, and S. A. Lee, Atom Interferometer Based on Bragg Scattering from Standing Light Waves, Phys. Rev. Lett. **75**, 2638 (1995).

[31] C. J. Bordé, Matter-wave interferometers: A synthetic approach, in *Atom Interferometry*, edited by P. R. Berman (Academic Press, San Diego, CA, 1997), pp. 257–292.

[32] M. Kozuma, L. Deng, E. W. Hagley, J. Wen, R. Lutwak, K. Helmerson, S. L. Rolston, and W. D. Phillips, Coherent Splitting of Bose-Einstein Condensed Atoms with Optically Induced Bragg Diffraction, Phys. Rev. Lett. **82**, 871 (1999).

[33] S. Gupta, A. E. Leanhardt, A. D. Cronin, and D. E. Pritchard, Coherent manipulation of atoms with standing light waves, C.R. Acad. Sci. Ser. IV: Phys. Astrophys. **2**, 479 (2001).

[34] S. M. Barnett and P. M. Radmore, *Methods in Theoretical Quantum Optics* (Clarendon Press, Oxford, UK, 1997).

[35] M. Saunders, P. L. Halkyard, K. J. Challis, and S. A. Gardiner, Manifestation of quantum resonances and antiresonances in a finite-temperature dilute atomic gas, Phys. Rev. A **76**, 043415 (2007).

[36] I. G. Hughes and T. P. A. Hase, *Measurements and Their Uncertainties* (Oxford University Press, New York, 2010).